https://doi.org/10.5194/egusphere-2026-6699
Preprint. Discussion started: 13 November 2026
© Author(s) 2026. CC BY 4.0 License.

Contrasting updraft–downdraft organization of turbulent heat transport across heights and underlying surfaces: evidence from three meteorological towers

Linlin Wang[1], Yuanjian Yang[2]*, Xueling Cheng[1], Miao Yu [3], Jiesheng Xue[2], Zhiqiu Gao[2], Bingcheng Wan[4], Yuhong Weng[1]

[1]Institute of Atmospheric Physics, Chinese Academy of Sciences, Beijing, China

[2]Collaborative Innovation Centre on Forecast and Evaluation of Meteorological Disasters, School of Atmospheric Physics, Nanjing University of Information Science and Technology, Nanjing, China

[3]State Key Laboratory of Severe Weather Meteorological Science and Technology, Chinese Academy of Meteorological Sciences, Beijing, China

[4]School of Artificial Intelligence (School of Future Technology), Nanjing University of Information Science and Technology, Nanjing, China

Correspondence to: Dr. Y. Yang, yyj1985@nuist.edu.cn

Abstract

Turbulent heat exchange shapes boundary-layer evolution, yet vertical heat-flux transport remains challenging over heterogeneous surfaces. At three towers — the Institute of Atmospheric Physics (IAP) in urban Beijing, mixed Xianghe, and peri-urban Miyun — we examine updraft–downdraft transport and implications for third-order moment closure. Across ten site–height combinations, normalized vertical-velocity variability rises with instability, while skewness and mixed third-order heat transport show height-dependent stability responses. The bulk second – third moment relationship remains identifiable. Exact decomposition identifies within-branch velocity – temperature covariance as the largest contributor to the temperature-related bulk-regression residual component at nine combinations. At IAP, median paired-hour 80 – 47 m differences in occupancy-weighted within-branch covariance are positive for updrafts and negative for downdrafts in 2014–2015. Simultaneous strong motions occupy 13–14% of paired samples but account for 66–76% of the signed mean covariance-imbalance height contrast. Triggered composites further reveal height-dependent amplitudes and evolution of velocity, temperature, and third-order transport. Across sites, warm anomalies at comparable normalized updraft speeds are larger under buoyancy-dominated than shear-dominated conditions. Afternoon updraft velocity – temperature correlation weakens at lower IAP and Miyun but persists at Xianghe and upper IAP. Measured within-branch covariance reduces reconstruction root-mean-square error by 50–60% against the branch-based reference. These findings demonstrate that the observed bulk second–third moment relationship does not uniquely constrain updraft–downdraft heat-flux organization across heights and surface environments.

https://doi.org/10.5194/egusphere-2026-6699
Preprint. Discussion started: 13 November 2026
© Author(s) 2026. CC BY 4.0 License.

Keywords: urban boundary layer; third-order moments; mass-flux closure; updraft–downdraft decomposition

1. Introduction

Urban roughness shapes the vertical distribution of mean shear, wake production and turbulent exchange, while heterogeneous surface heating modifies the temperature anomalies carried by vertical motions. These influences vary with height because canopy-scale motions can remain coherent above roughness elements and contribute differently to transport within and above the roughness sublayer (Raupach et al., 1996; Rotach, 1999; Finnigan, 2000; Roth, 2000). Urban observations and wind-tunnel experiments document corresponding changes in turbulence structure and transport across heights (Rotach et al., 2005; Barlow, 2014; Li et al., 2025). Heterogeneous heating can also alter the preferred locations of updrafts and downdrafts and the fluxes sampled by towers (De Roo and Mauder, 2018). Understanding heat exchange over these surfaces therefore requires examining how vertical motions couple with temperature fluctuations and how their contributions to transport change with height.

The kinematic sonic-temperature flux ($\overline{w'T_s'}$), measures the net vertical turbulent heat exchange at a given height. Its vertical turbulent transport is represented by the mixed third-order moment ($M \equiv \overline{w'^2 T_s'}$), whose negative vertical divergence enters the heat-flux budget. Here, T_s' denotes the sonic-temperature fluctuation used throughout this study. The two moments weight the same motions differently. Warm updrafts and cool downdrafts both contribute positively to $\overline{w'T_s'}$, but contribute with opposite signs to M, which also gives greater weight to stronger vertical motions. The magnitude of the net heat flux alone therefore does not determine its vertical turbulent transport. Observations and conditional analyses have linked scalar exchange to unequal contributions from coherent motions, while joint-distribution studies connect these contributions to mixed third-order moments (Kaimal et al., 1976; Katul et al., 1997; Ghannam et al., 2017; Li et al., 2018; Liu et al., 2021).

Higher-order closure theories relate this transport to the statistical properties of rising and sinking motions. Mass-flux approaches describe their fractional occupancy and conditional properties (Abdella and McFarlane, 1997; Lappen and Randall, 2001), while skewness-based formulations connect third-order heat-flux transport with the heat flux and vertical-velocity statistics (Zilitinkevich et al., 1999; Gryanik and Hartmann, 2002). The information retained within each population is important. Top-hat approximations neglect subplume fluctuations, which can lead to underestimation of third-order moments (Abdella and Petersen, 2000), and their performance differs between scalar fluxes, variances and mixed higher-order moments (Wang and Stevens, 2000). Two-fluid formulations explicitly distinguish transport within and between coherent structures (Efstathiou et al., 2020), while joint-PDF and generalized mass-flux approaches retain additional distributional information (Golaz et al., 2002; Larson and Golaz, 2005; Siebesma et al., 2007; Arnold et al., 2026; d'Alençon et al., 2026). These developments establish a physical basis for

https://doi.org/10.5194/egusphere-2026-6699
Preprint. Discussion started: 13 November 2026
© Author(s) 2026. CC BY 4.0 License.

examining both the contrasts between ascending and descending populations and the velocity–temperature fluctuations within them.

Barskov et al. (2023) found that a second–third moment relationship remained identifiable over grassland and urban surfaces even when individual moments departed from classical similarity functions. Its fitted coefficients and scatter nevertheless varied with measurement height and wind direction, with related variations reported by Drozd et al. (2023). The persistence of such a relationship raises the question of how consistently it represents heat-flux transport carried by different vertical motions across flow environments. Existing closure theories identify the conditional information relevant to this transport, but the observed bulk relationship does not establish how that information varies with height, surface environment or thermomechanical state. Examining bulk moments alongside conditional velocity–temperature distributions can therefore reveal how turbulent heat-flux transport is organized under these conditions and which aspects of that organization are represented by the overall moment relationship.

Using high-frequency observations from three meteorological towers, we investigate how vertical motions and their associated temperature fluctuations organize turbulent heat-flux transport across heights, surface environments and thermomechanical states. Seven sonic levels spanning 8–280 m at the Institute of Atmospheric Physics (IAP) site in central urban Beijing provide a detailed vertical profile over a densely built-up surface, while Xianghe and Miyun extend the comparison to mixed agricultural–developed and peri-urban environments. We first examine the stability dependence of turbulent moments and compare bulk second–third moment relationships across sites and heights. Exact updraft–downdraft decomposition and motion-intensity-resolved conditional statistics are then used to distinguish branch-mean and within-branch contributions and characterize their variations with height and thermomechanical state. Diagnostic reconstruction assesses the contribution of observed within-branch velocity–temperature covariance to the representation of the mixed third-order moment $\overline{w'^2T_s'}$.

2. Materials and methods

2.1 Sites and observations

The analysis combined high-frequency turbulence observations from three sites: the IAP site (39.97°N, 116.37°E) of the Chinese Academy of Sciences in central urban Beijing, Xianghe (39.75°N, 116.97°E) in Hebei Province, and Miyun (40.38°N, 116.86°E) in northeastern Beijing. Relative to the IAP tower, Xianghe lies approximately 56 km to the east-southeast and Miyun approximately 62 km to the northeast (straight-line distances). Measurements at the IAP site were made on a 325-m urban meteorological tower . The three-dimensional sonic measurements were available at 8, 16, 47, 80, 140, 200, and 280 m. The tower also provided multi-level slow-response wind speed (WS), wind direction (WD), and air temperature (T). The slow-response system used Met One 010C/020C wind sensors and Rotronic HC2-S3 temperature-humidity sensors. At Xianghe , 10-Hz WindMaster sonic measurements were available at 32 and 64 m; Miyun provided a 36-m three-dimensional sonic record. Table 1 lists the observation heights, ancillary measurements and analysis periods. The three-site comparison uses 2014 observations. IAP data from 2015 were

https://doi.org/10.5194/egusphere-2026-6699
Preprint. Discussion started: 13 November 2026
© Author(s) 2026. CC BY 4.0 License.

processed with the same definitions for the paired 47–80 m analysis and for testing the reconstruction against a bulk relationship calibrated in 2014. All times are China Standard Time (UTC+8).

We estimated source areas for the 2014 unstable-period flux observations with the two-dimensional Flux Footprint Prediction (FFP) model of Kljun et al. (2015), as shown in Fig. 1. The model inputs included height above displacement ($z_m = z - d$), site-specific aerodynamic roughness length z_0, observed friction velocity u_*, crosswind velocity standard deviation σ_v, wind direction and Obukhov length L, together with boundary-layer height (Hersbach et al., 2020). Hourly footprints were aggregated as two-dimensional climatologies. The 80% contours enclose the highest-density grid cells whose integrated modeled weights sum to 80% of the footprint, and were overlaid on the 2014 CLCD map. Land-cover area fractions and footprint-density-weighted fractions were evaluated within each contour. The implemented FFP screening required finite model inputs, $\sigma_v > 0$, a valid wind direction, $z_m/L > -15.5$, $z_m > 20z_0$, $z_m < 0.8h$ and $u_* > 0.1$ m s^{-1}, where h is the boundary-layer height from the fifth-generation European Centre for Medium-Range Weather Forecasts (ECMWF) atmospheric reanalysis (ERA5). The aerodynamic roughness lengths supplied to FFP were $z_0 = 4.14$ m at IAP, 0.61 m at Xianghe and 0.65 m at Miyun. Zero-plane displacement height d was estimated independently at IAP ($d = 18.35$ m), Miyun ($d = 4.15$ m), and Xianghe ($d = 0.70$ m) from near-neutral multilevel mean-wind profiles using a neutral logarithmic wind-profile fit. The method follows the anemometric approach applied to Miyun by Dou et al. (2019).

The surrounding land cover was characterized by using the 2014 China Land Cover Dataset (CLCD v1.0.0, 30 m resolution; Yang and Huang, 2021a,b; Fig. 1). The mapped domains were 22 × 22 km at IAP, 5 × 5 km at Xianghe and 2.5 × 2.5 km at Miyun, each enclosing the largest modeled 80% footprint contour available for that site. The resulting land-cover fractions characterize different domain sizes and should not be interpreted as equivalent source areas. IAP lies within nearly continuous urban development. Cropland occupies a substantial part of the Xianghe surroundings, interspersed with developed land; Miyun combines developed land near the tower with cropland, particularly to the east and southeast (Fig. 1). The two mixed-surface sites therefore differ not only in land-cover fractions but also in their spatial arrangement. Within the modeled 80% source areas, footprint-weighted impervious fractions were 99.6%, 99.2% and 97.9% at IAP 140, 200 and 280 m, 58.9% and 57.7% at Xianghe 32 and 64 m, and 67.6% at Miyun 36 m. These values confirm the predominantly impervious source areas at the eligible IAP heights and the mixed land-cover contributions at Xianghe and Miyun. Xianghe and Miyun have similar estimated aerodynamic roughness lengths but different displacement heights.

Table 1. Observational configuration at IAP, Xianghe, and Miyun sites.

Site	Period used	10-Hz sonic level	Slow-response level	Aerodynamic parameters
IAP	2014 main; 2015 paired structural and frozen-year tests	8, 16, 47, 80, 140, 200, 280 m	8, 15, 32, 47, 65, 80, 103, 120, 140, 160, 180, 200, 240, 280, 320 m	d = 18.35 m; z_0 = 4.14 m
Xianghe	2014	32 and 64 m	8, 15, 32, 47, 65, 80, 100 m	d = 0.70 m; z_0 = 0.61 m
Miyun	2014	36 m	10, 17, 24, 34 m	d = 4.15 m; z_0 = 0.65 m

https://doi.org/10.5194/egusphere-2026-6699
Preprint. Discussion started: 13 November 2026
© Author(s) 2026. CC BY 4.0 License.

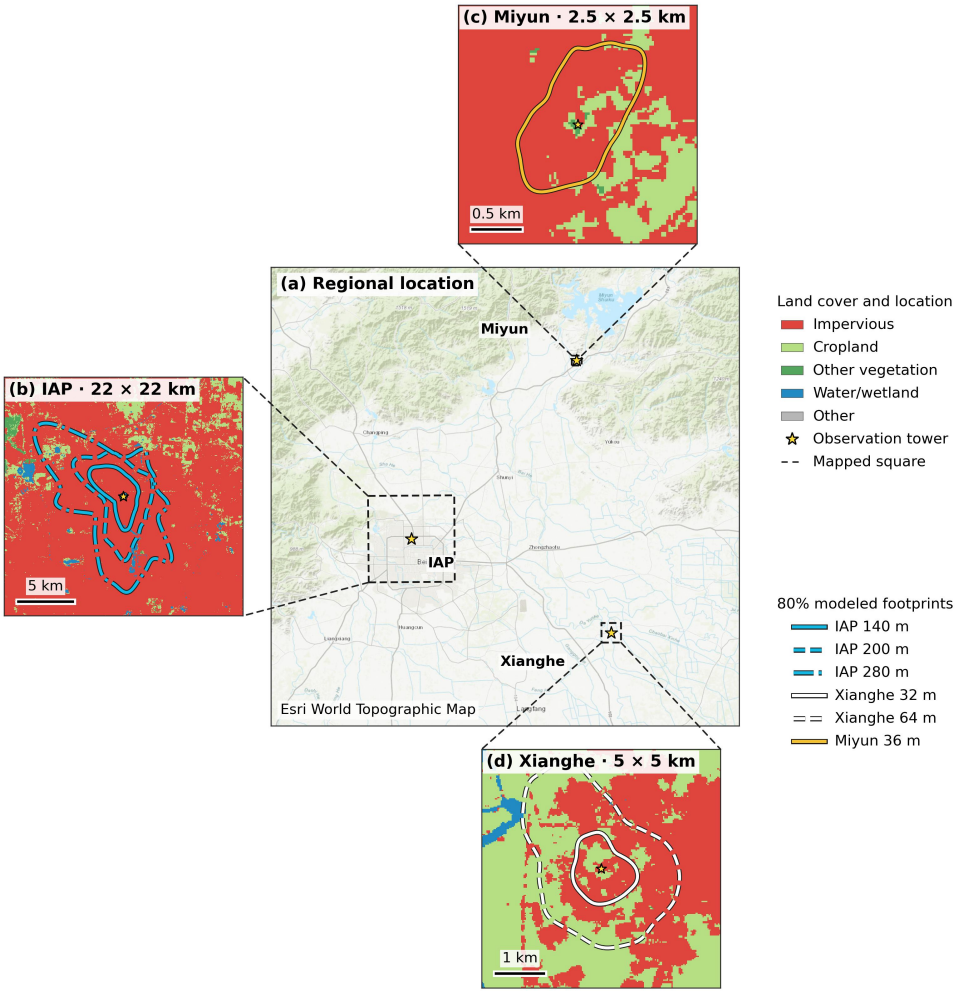


Fig. 1. Regional locations, 2014 land cover, and modeled 80% flux footprints. (a) Regional locations of IAP, Xianghe, and Miyun (Sources: Esri, TomTom, FAO, USGS | Powered by Esri); (b) IAP (22 × 22 km; 140, 200, and 280 m); (c) Miyun (2.5 × 2.5 km; 36 m); (d) Xianghe (5 × 5 km; 32 and 64 m). Stars mark towers; contours are modeled conventional flux footprints (Kljun et al., 2015). Land cover is from CLCD (Yang and Huang, 2021a,b).

2.2 Data processing

The 10-Hz sonic records were divided into non-overlapping 60-min intervals. Physical-range limits and instrument diagnostic flags were applied before despiking. An isolated discontinuity screen removed single-sample spikes at IAP and Xianghe without truncating sustained large-amplitude

https://doi.org/10.5194/egusphere-2026-6699
Preprint. Discussion started: 13 November 2026
© Author(s) 2026. CC BY 4.0 License.

motions. Miyun used the same physical checks together with an eight-median-absolute-deviation spike threshold.

Wind components were transformed into the mean-flow coordinate system by double rotation within each hour. Linear trends were removed independently from the rotated u, v, w, and sonic-temperature records. The residual hourly mean cross-wind and vertical velocities were each required to be within 0.02 m s^{-1} of zero. An hour was retained only when at least 90% of core samples were valid, the spike fraction did not exceed 1%, and coordinate rotation passed this check.

The principal turbulent moments were calculated from each retained, linearly detrended 60-min record as

$$F_T=\overline{w'T_s'}, \qquad W_2=\overline{w'^2}, \qquad W_3=\overline{w'^3}, \qquad M=\overline{w'^2T_s'}. \tag{1}$$

The vertical-velocity standard deviation, skewness, and sonic-temperature scale were defined by $\sigma_w = W_2^{1/2}$, $S_w = W_3/W_2^{3/2}$, and $T_* = F_T/u_*$, respectively. Following Barskov et al. (2023), T_* has the same sign as F_T. The vector friction velocity u_* was used in all normalized variables; detailed definitions are provided in Supplementary Methods S1. Nonstationarity was assessed separately for F_T, W_2, W_3, and M following Foken and Wichura (1996). Each 60-min estimate was compared with six independently detrended 10-min estimates. Every subwindow required at least 90% valid samples, and each of the four moment-specific nonstationarity ratios had to be no greater than 30%. The ratio $R_{N,Q}$ is defined in Supplementary Methods S1.

The local Obukhov length L was calculated from the vector friction velocity and kinematic sonic-temperature flux. The stability coordinate $\zeta = (z-d)/L$ used the site-specific displacement height d. Sonic temperature was used as a virtual-temperature approximation for this scaling; the calculation and constants are given in Supplementary Methods S1. At IAP 8 and 16 m, the uncorrected height-to-Obukhov-length ratio was used as an observational stability coordinate because both levels lie below the estimated displacement height; it was not treated as a formal surface-layer similarity test. Two instability subsets were defined. The unstable baseline ($\zeta <- 0.005$), following Barskov et al. (2023), was used to examine the stability dependence of turbulent moments. The strongly unstable subset ($\zeta <- 0.06$) was used for branch decomposition and thermomechanical comparisons, retaining only hours with complete conditional statistics. Analyses of the bulk second–third moment relationship and residual-conditioned transport, as well as calculations of normalized closure quantities, additionally required an identifiable heat-flux denominator. Specifically, all six independently evaluated 10-min heat-flux estimates had to be finite, and their 95% Student's t confidence interval had to exclude zero (Supplementary Methods S1). Single-height analyses used qualifying observations at each site and level, whereas paired-height comparisons included only hours valid at both heights.

2.3 Similarity and second–third moment closure

The stability dependence of the normalized mixed third-order heat-transport moment, vertical-velocity skewness, and normalized vertical-velocity standard deviation was compared with the unstable similarity relationships used by Barskov et al. (2023). These include the free-convection scaling of the mixed third-order moment and the reference functions for skewness and σ_w/u_*. The comparisons used the unstable baseline defined in Section 2.2.

https://doi.org/10.5194/egusphere-2026-6699
Preprint. Discussion started: 13 November 2026
© Author(s) 2026. CC BY 4.0 License.

The normalized second–third moment relationship and its velocity-asymmetry predictor follow Barskov et al. (2023):

$$Y_B = \frac{M}{u_*^2 T_*} = \frac{M}{u_* F_T} = a + C X_B. \tag{2a}$$

$$X_B = \frac{S_w \sigma_w}{u_*} = \frac{W_3}{u_* W_2}. \tag{2b}$$

The equivalent dimensional form is given in Supplementary Methods S1.

The relationship was fitted by ordinary least squares (OLS), allowing a free intercept a and slope C. The regression used all retained hours in the denominator-identifiable unstable sample (Section 2.2). Fit quality was evaluated using R^2, root-mean-square error (RMSE), and relative scatter R_S = RMSE/$(X_{\max} - X_{\min})$. Because the response is $M/(u_* F_T)$, OLS in normalized coordinates minimizes dimensional squared errors weighted by $1/(u_* F_T)^2$. The RMSE of dimensional reconstructions was evaluated without this weighting. Through-origin fits and shuffled-variable tests were also used as sensitivity analyses.

2.4 Branch decomposition and conditional thermal diagnostics

The kinematic sonic-temperature flux F_T and mixed third-order moment M were partitioned into updraft ($w' > 0$) and downdraft ($w' < 0$) branches. The third-order moment adds a vertical-velocity weight to instantaneous heat-flux transport. For branch j, p_j denotes occupancy, and $m_{w,j}$ and $m_{T,j}$ are the conditional means of w' and T_s'; tildes indicate within-branch deviations. Exact expansions separate branch-mean transport from within-branch covariance, variance loading and third-order tails (Supplementary Methods S2).

Subscript b denotes the branch-mean (top-hat) approximation and i its within-branch remainder, consistent with mass-flux decompositions of second- and third-order moments (Abdella and Petersen, 2000; Wang and Stevens, 2000). The departure from the unit-coefficient term kF_T is partitioned into thermal and velocity-asymmetry corrections; the empirical coefficient C in Eq. (2a) is fitted independently:

$$k = \frac{W_3}{W_2}, \qquad k_b = \frac{W_{3,b}}{W_{2,b}} \tag{3a}$$

$$E = M - kF_T = E_T + E_V. \tag{3b}$$

$$F_{T,i} = F_T - F_{T,b}, \qquad M_i = M - M_b \tag{4a}$$

$$E_T = M_i - k_b F_{T,i}, \qquad E_V = (k_b - k) F_T. \tag{4b}$$

The thermal correction E_T contains variance loading, within-branch velocity–temperature covariance and conditional-tail contributions, whereas E_V reflects the difference between full and branch-mean velocity asymmetry (Supplementary Methods S2).

Normalization gives

$$X_B = \frac{k}{u_*}, \quad Y_B = \frac{M}{u_* F_T} \tag{5a}$$

$$t = \frac{E_T}{u_* F_T}, \quad v = \frac{E_V}{u_* F_T} \tag{5b}$$

$$Y_B = X_B + t + v \tag{6}$$

https://doi.org/10.5194/egusphere-2026-6699
Preprint. Discussion started: 13 November 2026
© Author(s) 2026. CC BY 4.0 License.

At each site–height combination, regressing Y_B on X_B in the strongly unstable, branch-complete sample gives the fitted-slope departure

$$C - 1 = \frac{\mathrm{Cov}(X_B, t)}{\mathrm{Var}(X_B)} + \frac{\mathrm{Cov}(X_B, v)}{\mathrm{Var}(X_B)} \tag{7}$$

To allocate unexplained normalized variability, Y_B, t and v were separately residualized against X_B on identical observations using free-intercept regressions. The identity $r_Y = r_t + r_v$ then gives

$$P_T = \frac{\mathrm{Cov}(r_Y, r_t)}{\mathrm{Var}(Y_B)}, \qquad P_V = \frac{\mathrm{Cov}(r_Y, r_v)}{\mathrm{Var}(Y_B)} \tag{8a}$$

$$P_T + P_V = 1 - R^2 \tag{8b}$$

The allocations sum to $1 - R^2$, but the thermal–velocity residual cross-covariance enters each component allocation, so either may be negative or exceed the unexplained fraction. The thermal residual was further separated into within-branch variance loading, covariance and conditional tails, each residualized against X_B. Their signed shares sum to unity; uncertainty procedures are described in Supplementary Methods S2.

To resolve transport by motion intensity, each hour was standardized as $x = w'/\sigma_w$ and $\theta = T_s'/\sigma_T$. Fixed bins were evaluated separately for updrafts and downdrafts, with conditional temperature anomaly $\mu_{\theta,j}(x) = \mathrm{E}(\theta|x, j)$. The branch-weighted contribution density is

$$K_j(x) = x^2\, \mathrm{E}[\theta|x, j]p_j(x). \tag{9}$$

Here $p_j(x)$ is the full-hour probability density in branch j, and $\int K_j(x)\,dx$ is the branch contribution to $M/(\sigma_w^2\sigma_T)$. The top-hat reference uses $\left(m_{w,j}/\sigma_w,\, m_{T,j}/\sigma_T\right)$. Conditional anomalies and kernels were calculated for each hour and averaged with equal hourly weight. Displayed bins required at least 10 contributing hours and coverage of 10% of the relevant hourly group.

Residual-conditioned transport was examined by comparing the upper and lower quartiles of the fitted bulk residual at each site and height in the denominator-identifiable unstable sample. Binwise differences $\Delta\mu_{\theta,j}$ and ΔK_j describe conditional temperature and signed transport contrasts. Because the grouping residual contains the observed third-order moment, these are associated structures rather than independent causal contributions to the residual.

For paired IAP observations at 47 and 80 m, within-branch covariance was isolated using the two-branch identity. With zero full-hour mean vertical velocity, the ratio of branch-mean third to second velocity moments equals the sum of the conditional updraft and downdraft mean velocities. We define

$$J_u = p_u \mathrm{Cov}_u\left(w', T_s'\right), \qquad J_d = p_d \mathrm{Cov}_d\left(w', T_s'\right) \tag{10a}$$

$$A_T = J_u - J_d, \qquad A_w = m_{w,u} - m_{w,d}, \qquad E_{\mathrm{cov}} = A_w A_T. \tag{10b}$$

The J terms are occupancy-weighted within-branch covariances, not complete branch heat fluxes. Paired-height diagnostics used the normalized velocity separation, covariance imbalance and covariance correction: $\frac{A_w}{u_*}$, $\frac{A_T}{F_T}$, $\frac{E_{\mathrm{cov}}}{u_* F_T}$. Changes in the imbalance were attributed to branch occupancy, conditional velocity–temperature correlation, and within-branch velocity and temperature standard deviations (Supplementary Methods S2).

https://doi.org/10.5194/egusphere-2026-6699
Preprint. Discussion started: 13 November 2026
© Author(s) 2026. CC BY 4.0 License.

To assess the information added by measured within-branch covariance, we compared three diagnostic expressions. In Eq. (11a), the coefficient is branch-based, whereas F_T is the complete observed heat flux:

$$\widehat{M}_{\mathrm{branch}} = k_b F_T \tag{11a}$$

$$\widehat{M}_{\mathrm{cov}} = k_b F_T + E_{\mathrm{cov}} \tag{11b}$$

$$\widehat{M}_{\mathrm{bulk}} = a\, u_* F_T + C\, k F_T. \tag{11c}$$

At each IAP height, the bulk coefficients a and C were fitted using the 2014 strongly unstable, branch-complete sample and held fixed for 2015 evaluation. The branch-based and covariance-augmented expressions instead used observed 2015 branch statistics. All three were evaluated against dimensional M on identical hours. At Xianghe and Miyun, only the two coefficient-free expressions were assessed; error metrics and uncertainty procedures are detailed in Supplementary Methods S3.

2.5 Thermomechanical diagnostics

Mean vertical shear was calculated exclusively from the slow-response wind profile. Meteorological wind direction (the direction from which the wind blows) was converted to fixed eastward and northward components as $U = -WS\sin(WD)$ and $V = -WS\cos(WD)$. Local $\partial U/\partial z$ and $\partial V/\partial z$ at a sonic height were estimated from a linear fit to the nearest three slow-response levels; one-sided adjacent-level slopes were used at profile endpoints. Sonic hourly mean wind speed and direction were not used to define the mean shear.

The turbulent stress components were transformed back to fixed east–north coordinates using the stored rotation metadata. Following the shear- and buoyancy-production terms of the turbulent kinetic energy budget (Christen et al., 2009), the resolved vertical shear-transfer term and the sonic-temperature estimate of buoyancy production were calculated as

$$P_{S,z} = -\overline{u'w'}\frac{\partial U}{\partial z} - \overline{v'w'}\frac{\partial V}{\partial z}. \tag{12a}$$

$$B = \frac{g}{\overline{T}} F_T. \tag{12b}$$

Positive $P_{S,z}$ indicates local turbulent kinetic energy production by vertical shear, whereas negative values indicate transfer to the mean flow. The magnitude $|P_{S,z}|$ measures the strength of this transfer. The buoyancy estimate B uses the slow-response absolute temperature and kinematic sonic-temperature flux.

State contrasts were restricted to $B > 0$ and $P_{S,z} > 0$. A buoyancy-dominated hour satisfied $B > 2P_{S,z}$, whereas a shear-dominated hour satisfied $P_{S,z} > 2B$; intermediate hours were not assigned to either state. The factor-of-two separation was selected for the state contrasts in this study. The magnitude ratio $|P_{S,z}|/B$ was used to describe relative shear-transfer magnitude. Within-updraft thermal coupling was quantified as $r_u = \mathrm{corr}(w', T_s' | w' > 0)$ for each hour. Thermomechanical-state analyses used the strong-unstable subset with complete branch terms. Conditional state contrasts used the same equal-hour standardization and binning described in Section 2.4. Diurnal summaries were calculated for 08:00–18:00 local time using hourly medians; IAP combined 2014 and 2015, whereas Xianghe and Miyun used 2014.

https://doi.org/10.5194/egusphere-2026-6699
Preprint. Discussion started: 13 November 2026
© Author(s) 2026. CC BY 4.0 License.

2.6 Uncertainty and sensitivity analyses

The 47–80 m event diagnostics used the paired 10-Hz records retained for the branch-covariance comparison. Matched cores required simultaneous same-sign vertical-velocity fluctuations satisfying the two-level $1.5\sigma_w/0.5\sigma_w$ criterion. Event composites were triggered separately by 80 m extrema, without requiring a match at 47 m. Supplementary Methods S4 specifies the selection and averaging procedures. Each hour was treated as the sampling unit for high-frequency conditional summaries; different heights on the same tower were not treated as independent spatial replicates. We used 5,000 month-block bootstrap resamples for the exact decomposition. For paired 47–80 m contrasts, the reported estimates are medians of hourly 80−47 m differences, with calendar-day blocks resampled for two-sided 95% percentile intervals. The branch identity is exact within each hour, but medians of the separate branch and total contrasts need not add because medians are nonlinear. Diagnostic reconstructions were compared with paired day-block resampling on identical evaluation samples. The hourly scatterplot displays joint updraft–downdraft covariance changes, and the opposing-sign quadrant fraction was evaluated over those same paired hours.

Two targeted sensitivity tests evaluated the dependence on sample selection. The stationarity test removed only the criterion on M while retaining the other quality-control requirements (Table S1). The daytime test restricted the analysis to 08:00–18:00 local time to assess whether the IAP vertical contrast and branch-covariance changes persisted without nighttime hours (Table S3).

3. Results

3.1 Turbulent moments and bulk second-third moment relationships

Figs. 2 and 3 show that the three normalized turbulent moments respond differently to increasing instability. The normalized vertical-velocity standard deviation, σ_w/u_*, rises across all ten site–height combinations, although many observations fall below the reference similarity curve under stronger instability. By contrast, vertical-velocity skewness, S_w, and normalized mixed third-order heat transport, $M/(u_*F_T)$, exhibit greater differences in sign and scatter with height and site. Barskov et al. (2023) also reported negative vertical-velocity skewness and departures of individual moments from similarity references over an urban surface. Earlier urban observations also reported reduced normalized vertical-velocity variability relative to rural reference data (Roth, 1993). The present measurements resolve how these contrasting responses vary over a seven-level urban profile. At IAP, negative S_w and $M/(u_*F_T)$ are common at 8–47 m under weak instability, whereas positive values become more frequent with stronger instability (Fig. 2). Positive mixed third moments are more prevalent at 80–280 m, but the instability dependence of S_w becomes less distinct aloft, especially at 200–280 m, even as $M/(u_*F_T)$ retains an increasing tendency. In contrast, σ_w/u_* shows a broadly increasing instability response throughout the tower. Thus, the upper-level weakening of the skewness response is not accompanied by a comparable loss of instability dependence in either vertical-velocity variability or mixed third-order transport. The stability coordinate at IAP 8 and 16 m is observational because both levels lie below the estimated displacement height; their comparison with reference curves is not a formal surface-layer similarity test.

https://doi.org/10.5194/egusphere-2026-6699
Preprint. Discussion started: 13 November 2026
© Author(s) 2026. CC BY 4.0 License.

The two Xianghe levels show a similar height selectivity over a much shorter vertical interval (Fig. 3). Negative S_w and $M/(u_*F_T)$ occur frequently at 32 m under weak instability, while positive values are more prevalent at 64 m. At Miyun 36 m, positive values predominate through much of the sampled instability range, although the skewness response is more scattered than the increasing mixed third moment. The normalized velocity standard deviation increases with instability at both sites, without a corresponding uniform behavior of the higher-order moments. Hence, comparable measurement heights at Xianghe, Miyun and IAP do not imply comparable velocity asymmetry or heat-flux transport. The sites also differ in stability sampling, instrumentation and source areas, so the contrasts cannot be attributed uniquely to land cover. These contrasting stability responses motivate the examination of the bulk second–third moment relationship in Fig. 4.

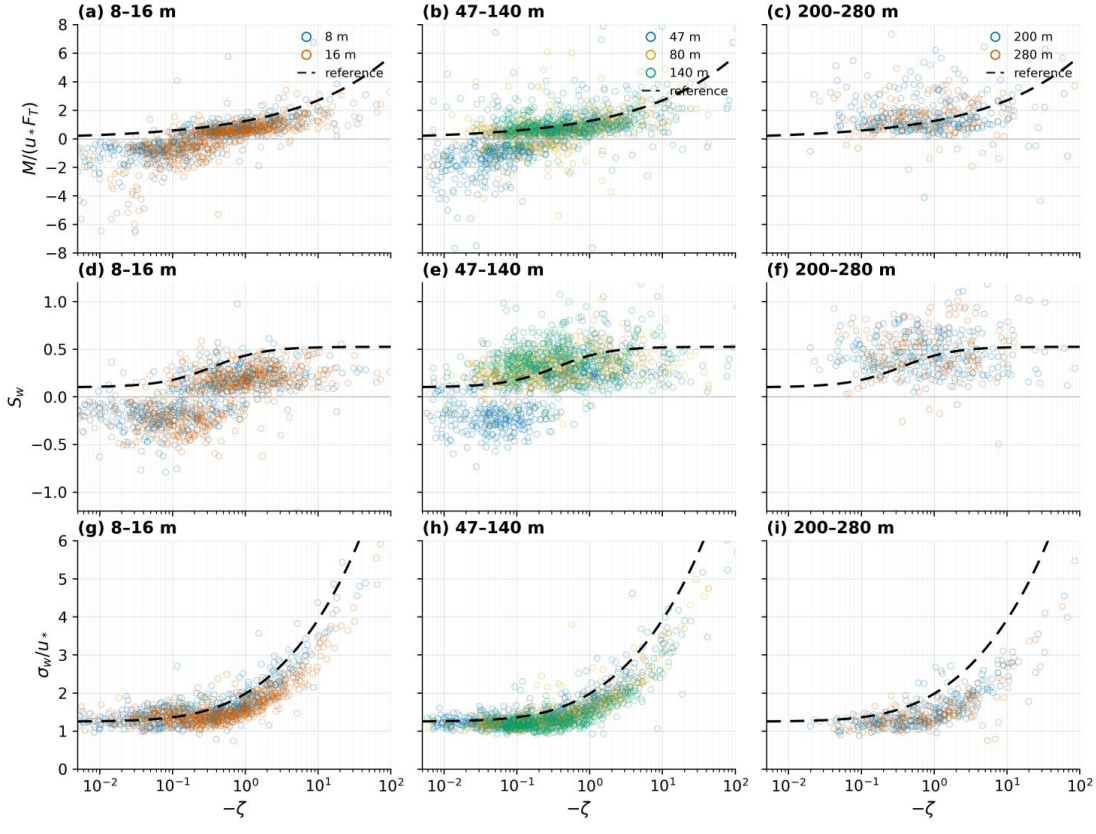


Fig. 2. Stability dependence of normalized turbulent moments at IAP. (a–c) Mixed third-order heat transport $M/(u_*F_T)$; (d–f) vertical-velocity skewness S_w; (g–i) normalized vertical-velocity standard deviation σ_w/u_*. Columns show 8–16, 47–140, and 200–280 m. Open symbols are hourly observations; dashed curves are similarity references (Barskov et al., 2023). The log-scaled abscissa is $-\zeta$.

https://doi.org/10.5194/egusphere-2026-6699
Preprint. Discussion started: 13 November 2026
© Author(s) 2026. CC BY 4.0 License.

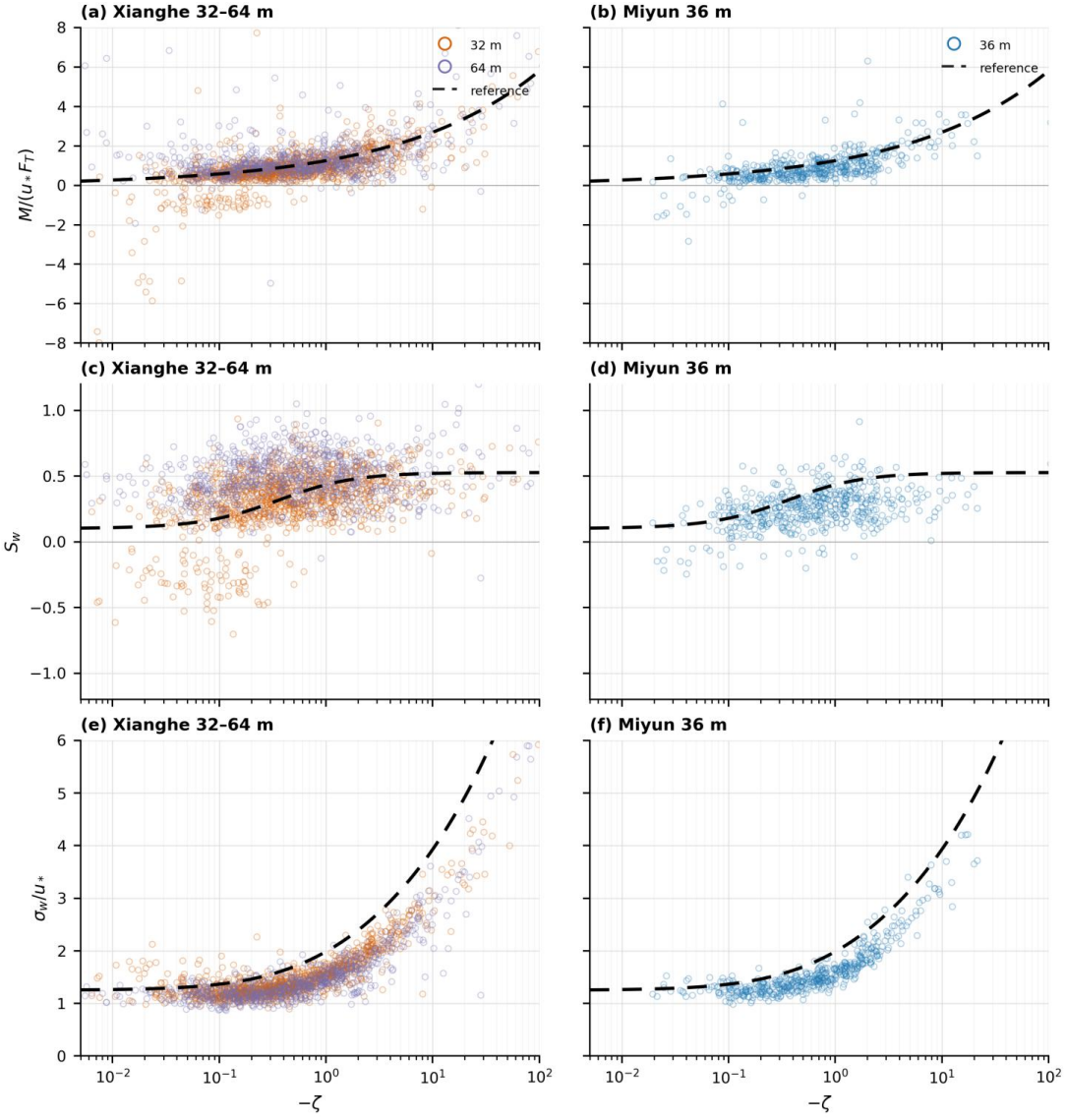


Fig. 3. Stability dependence of normalized turbulent moments at Xianghe (32 and 64 m) and Miyun (36 m). The variables, rows, and reference curves follow Fig. 2.

The bulk second–third moment relationship remains identifiable across all ten site–height combinations (Fig. 4), with fitted coefficients C ranging from 1.34 to 2.45 and R^2 from 0.38 to 0.75. This is consistent with the urban and grassland observations of Barskov et al. (2023) and the urban-tower assessment of Drozd et al. (2023). The seven-level IAP profile, however, reveals substantial vertical differences in fit quality: R^2 is 0.63, 0.69 and 0.71 at 8, 16 and 47 m, decreases to 0.45 at 80 m and 0.38–0.40 at 140–200 m, and increases again to 0.62 at 280 m. Meanwhile, (C) decreases from 2.16 at 47 m to 1.34 at 200 m before increasing to 2.45 at 280 m, indicating that the

https://doi.org/10.5194/egusphere-2026-6699
Preprint. Discussion started: 13 November 2026
© Author(s) 2026. CC BY 4.0 License.

fitted coefficient and goodness of fit do not vary together. Across sites, R^2 is 0.70 and 0.75 at Xianghe 32 and 64 m, respectively, compared with 0.52 at Miyun 36 m. Notably, Xianghe 32 m and IAP 80 m have nearly identical slopes (1.84 and 1.85) but different R^2 values (0.70 and 0.45). Thus, neither the IAP profile nor the cross-site comparison follows a simple ordering by height or degree of urban development. The fitted relationship is also sensitive to nonstationarity screening. Removing only the stationarity criterion on M increases the retained sample but lowers R^2 at every site–height combination, with the largest reduction at Xianghe 64 m, where R^2 falls from 0.75 to 0.41 (Table S1). The fitted coefficients remain broadly similar under this relaxation. These results show that the bulk relationship can persist despite substantial hourly scatter, while neither the fitted coefficient nor the scatter reveals how vertical motions and their associated temperature fluctuations contribute to third-order transport. Previous joint-distribution analyses have linked ejection–sweep asymmetry in scalar transport to mixed third-order moments (Ghannam et al., 2017), motivating the examination of conditional velocity–temperature contributions in Section 3.2.

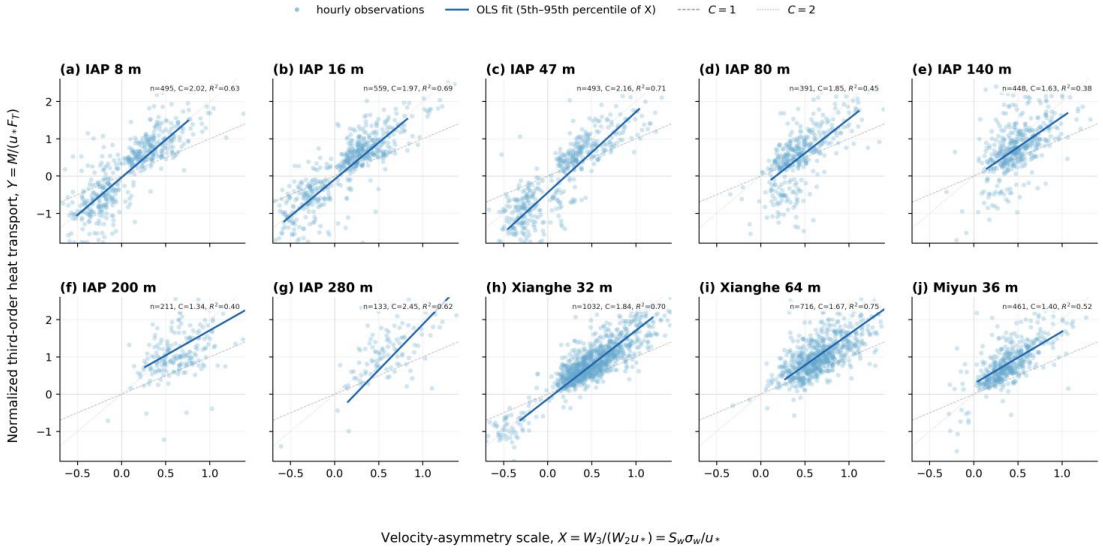


Fig. 4. Normalized second–third moment relationships at IAP, Xianghe, and Miyun. Points are hourly observations; solid lines are free-intercept OLS fits. Reported n, C, and R^2 and fitted lines use all retained hours, including those outside the displayed limits. For display, the OLS lines span the 5th–95th percentiles of X. Dashed and dotted lines mark reference slopes $C = 1$ and $C = 2$, respectively.

3.2 Branch-resolved organization of turbulent heat transport

Fig. 5 shows how different contributions underlie the fitted bulk second–third moment relationship. Across all ten site – height combinations, the temperature-related correction makes a positive contribution to the slope departure $C - 1$, while the velocity-asymmetry correction contributes negatively (Fig. 5a). Their partial compensation varies across sites and heights. The positive temperature-related contribution is particularly large at IAP 280 m, although its uncertainty is also substantial. The two corrections also differ in their contributions to unexplained variability. After removing the fitted dependence on the bulk predictor, the temperature-related correction accounts

https://doi.org/10.5194/egusphere-2026-6699
Preprint. Discussion started: 13 November 2026
© Author(s) 2026. CC BY 4.0 License.

for nearly all of the allocated unexplained variability at most site–height combinations (Fig. 5b). The variance of the velocity-asymmetry residual alone represents only 0.5–1.9% of the bulk-regression residual variance (Table S2). The allocations in Fig. 5b additionally include residual cross-covariance, as defined in Eq. (8).

Within the temperature-related component of the bulk-regression residual, within-branch velocity–temperature covariance has the largest point-estimate signed allocation share at nine of the ten site–height combinations (Table S4). At IAP 8–80 m, its share is 0.62–0.66, compared with 0.35–0.37 for conditional third-order tails. The covariance share decreases to 0.60 at 140 m and 0.58 at 200 m, while the tail share increases to 0.41 and 0.44, respectively. At 280 m, the point estimates are 0.27 for covariance and 0.76 for conditional tails. Covariance also has the largest share at Miyun 36 m (0.66) and Xianghe 32 and 64 m (0.65 and 0.59). Variance loading contributes little across the ten combinations. These signed shares partition the temperature-related residual component, not the total unexplained variance. Thus, within-branch covariance is an important contributor across all three sites, while conditional third-order tails become relatively more important at higher IAP levels. Their apparent predominance at 280 m remains uncertain because the bootstrap intervals overlap.

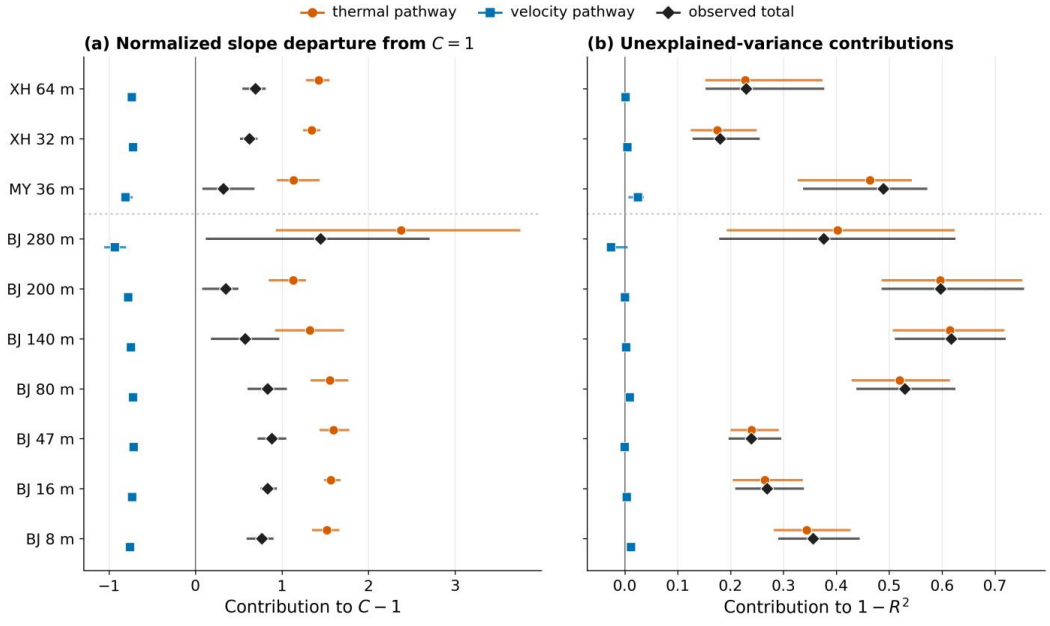


Fig. 5. Decomposition of the normalized second–third moment relationship at IAP, Miyun, and Xianghe. (a) Thermal and velocity-asymmetry contributions to the fitted slope departure $C - 1$; (b) contributions to unexplained variance $1 - R^2$. Black symbols indicate the totals; horizontal intervals show bootstrap uncertainty. Regressions use the strongly unstable, branch-complete sample.

Fig. 6 resolves this internal organization by motion intensity. At IAP, the branch-mean updraft reference lies near $|w'|/\sigma_w$ = 0.7–0.9, while the largest positive signed contributions to M

https://doi.org/10.5194/egusphere-2026-6699
Preprint. Discussion started: 13 November 2026
© Author(s) 2026. CC BY 4.0 License.

generally occur at stronger motions around $|w'|/\sigma_w$ = 1.5–2.2. Downdraft kernels similarly reach their negative extrema at speeds beyond their branch-mean reference, typically at normalized magnitudes near 1.0–2.0. Thus, the motions making the largest signed third-order contributions are stronger than the branch-mean motions, but are not simply the most extreme velocities plotted. The displacement of these transport maxima from the branch-mean speeds is consistent with LES-based mass-flux analyses in which subplume transport is not fully represented by a top-hat approximation (Petersen et al., 1999). The conditional temperature distributions show pronounced height dependence within the same velocity classes (Fig. 6). At IAP 8–16 m, the normalized warm anomalies in updrafts approach about 0.6 by a normalized speed of 1.5 and change relatively little at higher speeds (Fig. 6a). The middle levels separate more strongly: toward the highest displayed updraft speeds, the anomalies are about 0.65, 0.8 and 0.95 at 47, 80 and 140 m, respectively (Fig. 6b). At 200–280 m, the two updraft profiles remain relatively close to each other and continue rising, exceeding 1.3 near the upper end of the displayed speed range (Fig. 6c). Thus, neither the magnitude nor the velocity dependence of the conditional warm anomaly changes monotonically along the entire tower.

The downdraft structure differs from the updraft pattern. At 8–16 m, cool anomalies remain near −0.5 across a broad range of descending speeds (Fig. 6d). At the middle levels, 47 m has substantially more negative anomalies than 80 or 140 m once the normalized downward-speed magnitude exceeds about 2.0 (Fig. 6e); the 200 and 280 m profiles are comparatively similar (Fig. 6f). Despite these differences at strong velocities, the signed contribution kernels in both branches peak mainly at intermediate magnitudes, reflecting the combined roles of conditional temperature and the occurrence of each velocity class. The residual-quartile contrasts in Fig. S2 likewise show associated differences in conditional temperature and signed transport kernels. The different height dependences of updraft and downdraft temperature anomalies (Fig. 6), together with earlier observations of height-dependent sweep–ejection transport in urban roughness sublayers (Christen et al., 2007), motivate the paired 47–80 m analysis of within-branch covariance.

https://doi.org/10.5194/egusphere-2026-6699
Preprint. Discussion started: 13 November 2026
© Author(s) 2026. CC BY 4.0 License.

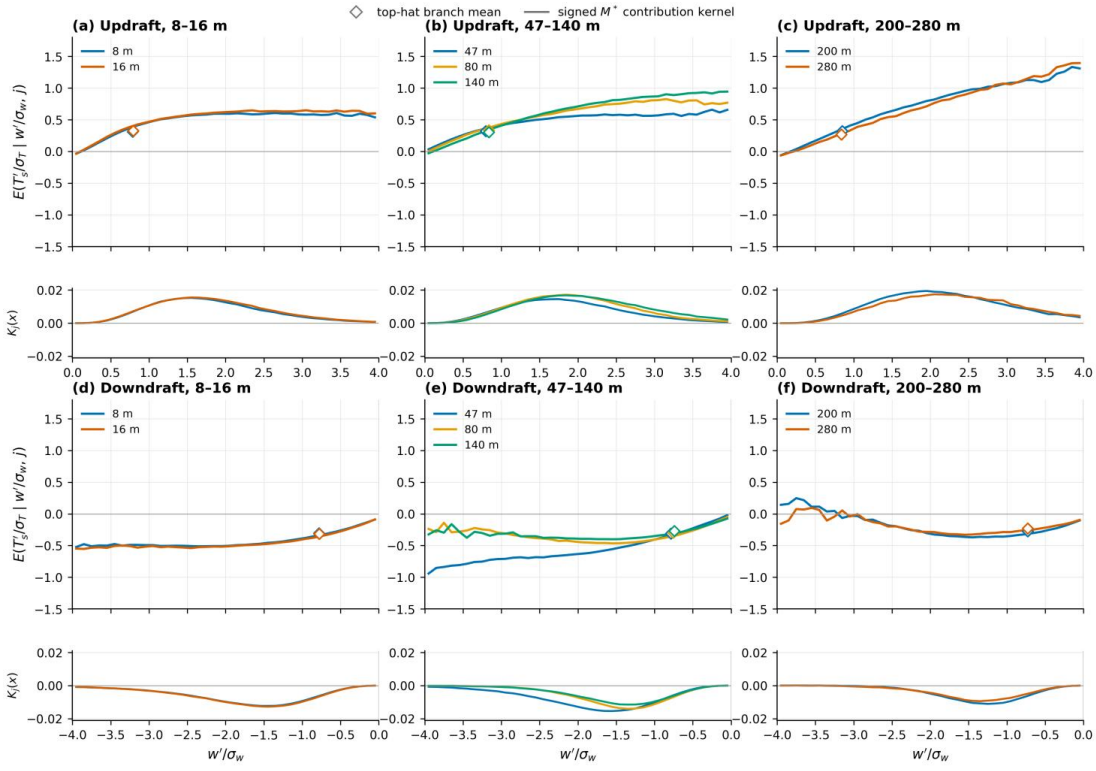


Fig. 6. Conditional temperature anomalies and signed third-order heat transport at IAP. (a–c) Updrafts; (d–f) downdrafts; columns represent 8–16, 47–140, and 200–280 m. Main curves show $E\left[T_s'/\sigma_T | w'/\sigma_w\right]$; lower curves show the signed contribution kernels $K_j(x)$. Open diamonds mark the branch-mean values used in the top-hat approximation; colors distinguish heights. The abscissa is w'/σ_w.

3.3 Paired-height covariance contrasts and third-order heat transport

Earlier measurements at IAP documented ejection-dominated momentum and scalar exchange under unstable conditions at 47, 140 and 280 m (Wang et al., 2014). The paired 47 and 80 m observations examine how velocity–temperature coupling within the two vertical-velocity sign branches changes across the urban profile. The median paired-hour 80−47 m contrast was positive for occupancy-weighted updraft covariance and negative for downdraft covariance in both 2014 (84 h) and 2015 (90 h; Fig. 7a). The inset shows positive median height contrasts in normalized covariance imbalance and the corresponding third-order covariance correction, without a consistent median increase in branch-mean vertical-velocity separation. The conditional velocity–temperature correlation makes the largest positive statistical contribution to the change in covariance imbalance (Fig. S1). The vertical adjustment therefore primarily concerns coupling within the branches rather than a uniform strengthening of their mean motions.

The covariance contrast was accompanied by height-dependent changes in measured turbulence and mean flow. In the common 47, 80 and 140 m samples (84 h in 2014 and 88 h in 2015), the increase in level-median vertical-velocity standard deviation was larger across 47–80 m than across 80–140

https://doi.org/10.5194/egusphere-2026-6699
Preprint. Discussion started: 13 November 2026
© Author(s) 2026. CC BY 4.0 License.

m: 0.045 versus 0.026 m s^{-1} in 2014 and 0.049 versus 0.017 m s^{-1} in 2015. The median gradient of hourly mean WS was likewise greater across 47–80 m (10.66 versus 9.03 × 10^{-3} s^{-1} in 2014 and 11.29 versus 7.92 × 10^{-3} s^{-1} in 2015). Christen et al. (2009) documented height-dependent balances of shear production and turbulent transport in an urban roughness sublayer. Here, the larger increase in vertical-velocity standard deviation and the greater mean WS gradient across 47–80 m provide the measured dynamical context for the branch-covariance changes in Fig. 7a.

The mean signed imbalance contrast, $\Delta A_T = \Delta J_u - \Delta J_d$, was concentrated in matched strong-motion cores (Fig. 7b). The 47 and 80 m fluctuations were required to have the same sign at each synchronized 10-Hz sample, with $|w'| \geq 1.5\sigma_w$ at one height and $|w'| \geq 0.5\sigma_w$ at the other; neither temperature nor covariance was used to select them. Cores occupied 13.7% of the sampled time in 2014 and 13.4% in 2015 but contributed 76.0% and 66.0% of the signed mean ΔA_T, respectively. The paired day-block bootstrap intervals for the core-minus-non-core net contrast were [1.10, 3.11] × 10^{-3} K m s^{-1} in 2014 and [0.57, 3.27] × 10^{-3} K m s^{-1} in 2015. The downdraft contrast was resolved in both years; the updraft contrast was not individually resolved in 2015.

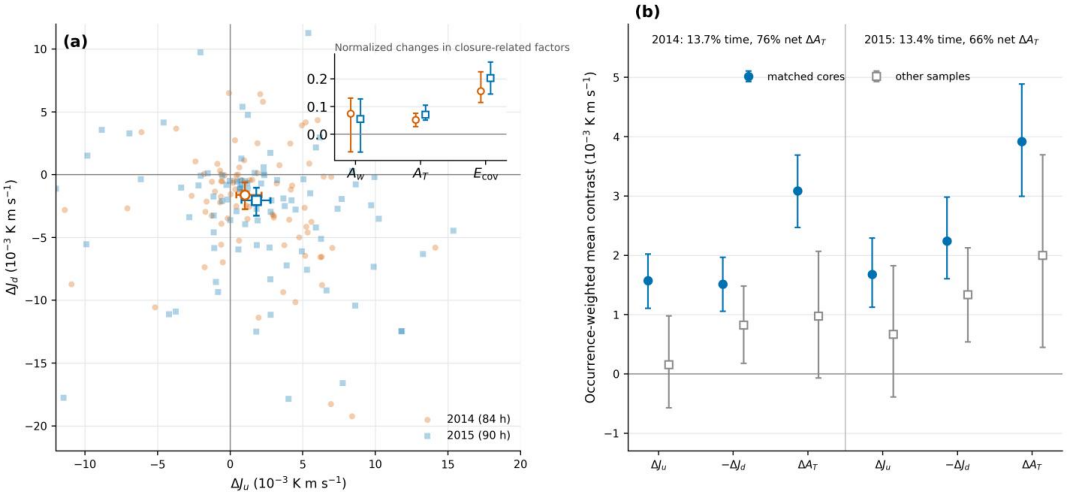


Fig. 7. 47–80 m changes in within-branch covariance at IAP. (a) Paired-hour contrasts ΔJ_u (horizontal) and ΔJ_d (vertical) for 2014 (84 h) and 2015 (90 h). Large open symbols are marginal medians with 95% day-block bootstrap intervals. The inset shows normalized contrasts $\Delta(A_w/u_*)$, $\Delta(A_T/F_T)$, and $\Delta[E_{cov}/(u_* F_T)]$. (b) Occurrence-weighted mean contributions of simultaneous strong-motion cores (blue) and other samples (grey) to ΔJ_u, $-\Delta J_d$, and ΔA_T, with 95% day-block bootstrap intervals. Core selection is defined in Supplementary Methods S4. All paired hours were included in the estimates; 1 point in 2014 and 3 points in 2015 lie outside the displayed limits of panel (a).

The vertical-velocity correlation between 47 and 80 m peaks near zero lag in both years (Fig. 8a). Composites triggered by 80 m velocity extrema show same-sign vertical motions at both heights, but their peak magnitudes and temporal profiles differ (Fig. 8b). The associated temperature anomalies also differ in amplitude and evolution between heights and between updraft and

https://doi.org/10.5194/egusphere-2026-6699
Preprint. Discussion started: 13 November 2026
© Author(s) 2026. CC BY 4.0 License.

downdraft events (Fig. 8c). The corresponding composites of instantaneous w'^2T_s' exhibit event-centred peaks with different amplitudes and temporal envelopes at the two heights. Warm-updraft events contribute positive w'^2T_s', whereas cool-downdraft events contribute negative values (Fig. 8d), even though both can contribute positively to $w'T_s'$ (Fig. S4). The opposite signs of the mixed third-order contributions arise because the squared vertical-velocity weighting preserves the sign of the temperature anomaly. The observed differences in peak magnitudes and temporal evolution between heights provide the more distinctive information. Earlier ejection–sweep analyses linked scalar-flux asymmetry to mixed third-order transport (Li et al., 2018; Liu et al., 2021). The present composites add a simultaneous two-height view of the conditional velocity and temperature structure. Reversing the trigger from 80 to 47 m also reverses the ordering of the updraft temperature peaks (Fig. S5), indicating that the event-centred height contrast depends on the triggering level. Unlike the simultaneous velocity-matched cores in Fig. 7b, the independently triggered composites in Fig. 8 characterize the event-conditioned velocity and temperature structures at the two heights. The paired covariance-height contrasts in Fig. 7 and the event-conditioned amplitudes and temporal responses in Fig. 8 therefore describe complementary aspects of the height-dependent organization of heat-flux transport.

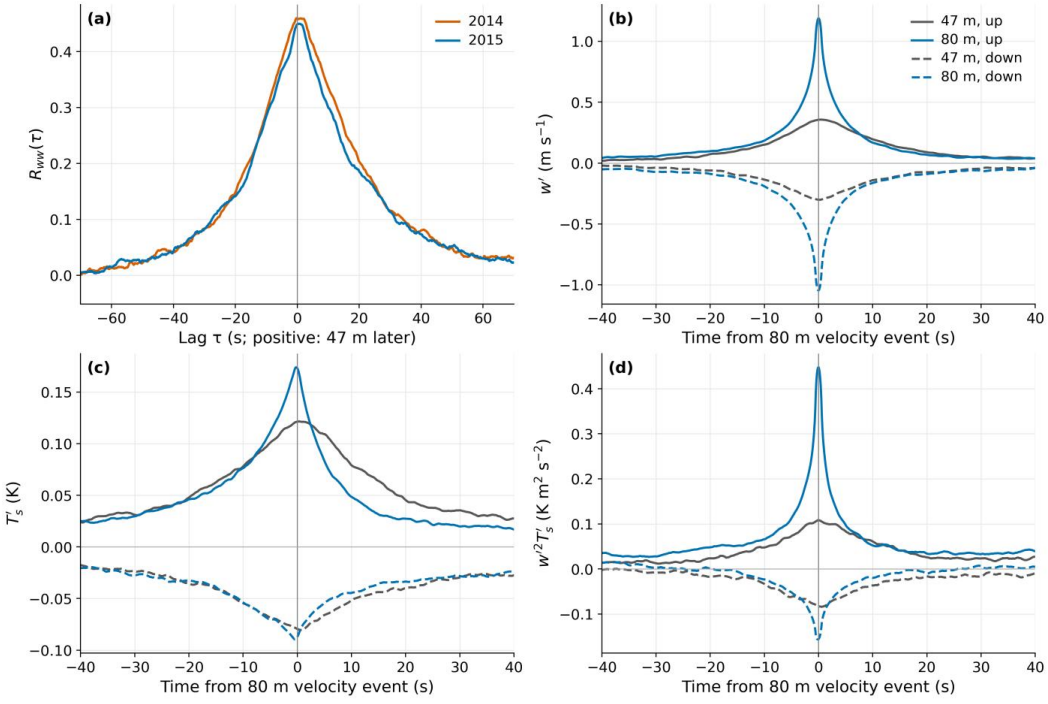


Fig. 8. Cross-height vertical-motion correlation and 80 m-triggered composites at IAP. (a) Lag correlation $R_{ww}(\tau)$ between 47 and 80 m in 2014 and 2015; positive lag indicates a later 47 m response. (b–d) Composites of w', T_s', and instantaneous w'^2T_s', respectively, for 2014–2015. Solid/dashed curves denote updraft/downdraft triggers; grey/blue denote 47/80 m. Composites give equal weight to qualifying hours. These events differ from the matched cores in Fig. 7b.

https://doi.org/10.5194/egusphere-2026-6699
Preprint. Discussion started: 13 November 2026
© Author(s) 2026. CC BY 4.0 License.

We evaluated the diagnostic contribution of within-branch covariance using the separate-year IAP 2015 records, with branch statistics measured during each evaluated hour (Eqs. (11a)–(11c); Table 2 and Fig. S3). Adding measured branch covariance lowered RMSE by 52.4–60.4% relative to the branch-based reference across seven heights, with paired day-block confidence intervals for the RMSE reduction entirely above zero at every height. It also improved over the 2014-fitted bulk relation at 8–80 m (17.8–40.5%), but not at 200 m; differences at 140 and 280 m were uncertain. At Miyun 36 m, covariance augmentation reduced RMSE by 57.4% relative to the branch-based reference; the corresponding reductions were 55.4% at Xianghe 32 m and 50.3% at Xianghe 64 m (Table 2). These are coefficient-free reconstructions using local 2014 branch statistics, not frozen-year prediction tests. The daytime-restricted analysis retained the IAP reduction in bulk closure fidelity, the opposing 47–80 m branch contrasts and the residualized thermal contribution (Table S3).

Table 2. Performance of the covariance-augmented reduced-order approximation in the IAP cross-year test and at Xianghe and Miyun.

Site / height	N	RMSE branch baseline	RMSE covariance-augmented	RMSE frozen bulk	Skill vs branch baseline (%)	Skill vs frozen bulk (%)
IAP 8 m	309	1.35	0.63	0.83	53.5	25.0
IAP 16 m	451	1.75	0.81	0.99	53.5	17.8
IAP 47 m	332	3.61	1.43	1.82	60.4	21.6
IAP 80 m	390	3.54	1.52	2.55	57.2	40.5
IAP 140 m	358	5.42	2.58	2.35	52.4	-9.7
IAP 200 m	197	4.89	2.27	1.83	53.6	-23.9
IAP 280 m	118	5.51	2.55	3.01	53.8	15.5
Miyun 36 m	451	2.85	1.21	—	57.4	—
Xianghe 32 m	973	2.19	0.98	—	55.4	—
Xianghe 64 m	676	3.17	1.58	—	50.3	—

Note. RMSE values are reported in 10^{-2} K m^2 s^{-2}. N is the common evaluation sample. Skill is the percentage reduction in RMSE of the covariance-augmented approximation relative to the stated reference, so positive values indicate lower error. IAP values use observed 2015 branch statistics, while only the bulk baseline uses height-specific coefficients fitted in 2014. Miyun and Xianghe values are 2014 coefficient-free comparisons based entirely on local branch statistics; no frozen-year bulk comparison was performed at these sites. — indicates that the frozen-year bulk comparison was not available.

3.4 Thermomechanical dependence of conditional heat transport

Fig. 9 compares the temperature anomalies carried by updrafts of comparable normalized intensity under buoyancy-dominated and shear-dominated conditions. Buoyancy-dominated hours exhibited larger warm anomalies, with the two conditional profiles separating most clearly above normalized updraft speeds of approximately 1.0–1.5. At IAP 80 m and Xianghe 32 m, warm anomalies continued to increase under buoyancy-dominated conditions while the shear-dominated responses became much flatter. At IAP 140 m and Miyun 36 m, both profiles increased with velocity, but their separation widened at stronger speeds. The buoyancy-minus-shear differences in integrated updraft contributions were +0.25 at IAP 80 m, +0.17 at IAP 140 m, +0.12 at Miyun 36 m, and +0.23 at

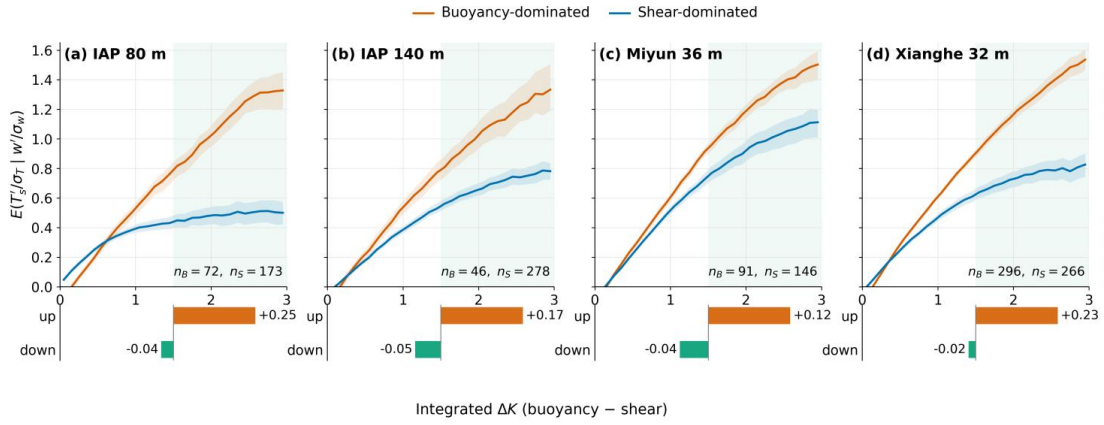
https://doi.org/10.5194/egusphere-2026-6699
Preprint. Discussion started: 13 November 2026
© Author(s) 2026. CC BY 4.0 License.

Xianghe 32 m. The corresponding buoyancy-minus-shear differences in integrated downdraft contributions were negative and much smaller in magnitude (−0.04, −0.05, −0.04, and −0.02, respectively). Conditional measurements have distinguished shear-organized motions from buoyant-plume contributions to scalar transport (Dupont and Patton, 2012). Urban-array LES further shows that surface heating produces plume-shaped structures and modifies the vertical organization of coherent motions above and within the building array (Park and Baik, 2013).

The daytime IAP profile reveals pronounced height dependence in the evolution of buoyancy production, relative vertical shear transfer, and thermal coupling within updrafts (Fig. 10). Buoyancy production at 47–140 m reached approximately 3.1–3.5 × 10^{-3} m^2 s^{-3} around late morning to midday and subsequently declined. At IAP 8–80 m, the decrease after approximately 13:00–14:00 LT coincided with increasing relative vertical shear-transfer magnitude and a reduction in within-updraft correlation from approximately 0.25–0.35 near midday to 0.03–0.16 at 15:00–16:00 LT. The decline was weaker at 140 m, while correlations at 200–280 m generally remained near 0.25–0.30 during the sampled afternoon. The late-day increase in relative shear-transfer magnitude was also less evident at the upper levels. Urban LES has shown that overlying large-scale coherent motions strongly modulate canopy-level momentum transport, whereas vertical heat flux is less sensitive to urban roughness under strongly convective conditions (Zhou et al., 2023). The IAP observations further show that the association between relative shear-transfer magnitude and within-updraft thermal coupling varies with height (Fig. 10).

The within-updraft correlations in Fig. 10c show different daytime evolutions across the three towers. At Miyun 36 m, the correlation was approximately 0.40 in the morning but decreased from late morning onward, reaching about 0.20–0.25 during the afternoon as buoyancy production diminished. At Xianghe 32 m, the correlation increased toward 0.35–0.40 around midday and remained near or above 0.30 through much of the afternoon. Xianghe 64 m likewise maintained values around 0.30–0.35 during midday and early afternoon. Although relative shear-transfer magnitude increased late in the day at Xianghe, its within-updraft correlation did not exhibit the pronounced afternoon decrease observed at IAP 47–80 m. These site- and height-dependent variations in within-updraft thermal coupling complement the heat–momentum transport dissimilarity previously documented using full-signal observations at IAP 140 m and Xianghe 32 m (Sun et al., 2026).

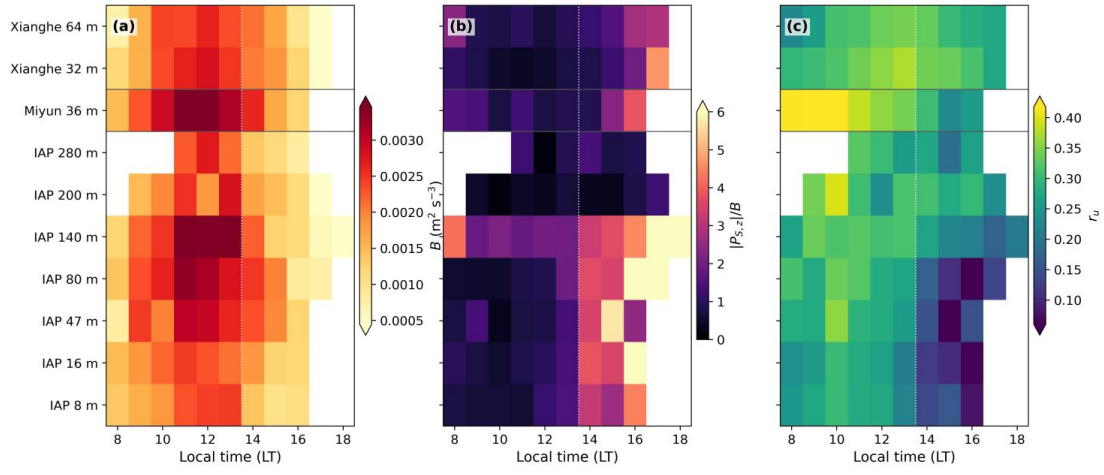
https://doi.org/10.5194/egusphere-2026-6699
Preprint. Discussion started: 13 November 2026
© Author(s) 2026. CC BY 4.0 License.



586

587 **Fig. 9.** Conditional updraft temperature anomalies under contrasting thermomechanical states. (a–d) E $\left[T_s'/\sigma_T|w'/\right.$
588 $\left.\sigma_w\right]$ at IAP 80 m, IAP 140 m, Miyun 36 m, and Xianghe 32 m for buoyancy- and shear-dominated hours. Shading
589 shows pointwise 95% day-block bootstrap intervals; pale green denotes $1.5 \leq w'/\sigma_w \leq 3.0$. Bars show
590 buoyancy-minus-shear integrated contributions ΔK for updrafts and downdrafts over their full available velocity
591 ranges.

592



593

594 **Fig. 10.** Diurnal variation of (a) buoyancy production B, (b) relative vertical shear-transfer magnitude $|P_{S,z}|/B$,
595 and (c) within-updraft thermal coupling r_u at IAP, Miyun, and Xianghe. Hourly medians are shown for
596 08:00–18:00 local time; white cells indicate fewer than 10 valid hours. The color ranges for buoyancy production
597 and within-updraft thermal coupling are set by the 2nd–98th percentiles of the pooled displayed cells. The relative
598 shear-transfer magnitude is displayed on a fixed 0–6 color scale; values outside the respective color limits are
599 saturated.

600 # 4. Discussion

601 ## 4.1 Updraft–downdraft structure and higher-order heat transport

602 The coexistence of an identifiable bulk second–third moment relationship with contrasting stability
603 responses of its constituent moments does not imply a common internal transport structure. At IAP,

https://doi.org/10.5194/egusphere-2026-6699
Preprint. Discussion started: 13 November 2026
© Author(s) 2026. CC BY 4.0 License.

the fitted coefficient and the scatter about the relationship vary differently with height (Fig. 4). The similar slopes but different R^2 values at Xianghe 32 m and IAP 80 m demonstrate that comparable average proportionality does not imply a similar fraction of explained hourly variability. Nor does the relatively tight relationship at IAP 280 m establish similarity with the internal transport structure below it. The exact decomposition helps explain this distinction. Thermal and velocity-asymmetry corrections partly offset one another in the fitted coefficient, whereas the temperature-related correction dominates the allocation of unexplained variance (Fig. 5). This distinction matters for conditional-mean closures. A top-hat representation reduces each branch to its conditional means, an approximation that has been found to reproduce scalar fluxes more consistently than some higher-order moments (Wang and Stevens, 2000). The exact expansion retains within-branch covariance, variance loading and conditional third-order tails. The predominance of within-branch covariance across nine site–height combinations, alongside its changing relative contribution along the IAP profile, highlights both shared and height-dependent features of the internal transport structure (Fig. 5; Table S4). The strongest signed third-order transport contributions occur away from the branch-mean velocities (Fig. 6), further demonstrating why conditional means alone cannot represent the full transport organization.

The thermomechanical contrasts show why the intensity of a vertical motion and the temperature anomaly it carries cannot be treated as interchangeable descriptors of heat transport. At comparable normalized updraft speeds, buoyancy-dominated conditions retain larger warm anomalies than shear-dominated conditions (Fig. 9). This distinction is consistent with observations and simulations showing that momentum and scalar transport have different responses to instability, coherent motions and turbulent scales (Li and Bou-Zeid, 2011; Sun et al., 2026). Mechanical roughness can modify the shear environment and the organization of vertical motions, whereas surface energy partitioning and heterogeneous heating set different thermal contrasts for those motions to carry (Miao et al., 2012; Wang et al., 2015; Theeuwes et al., 2019). The diurnal observations provide a complementary constraint: within-updraft thermal coupling weakens during the afternoon at the lower IAP levels and Miyun but persists longer at Xianghe (Fig. 10).

The urban tower provides a more direct test of how that conditional organization changes between vertically distinct flow environments above a densely built-up surface. Earlier studies associate 47 m at IAP with roughness-affected flow and approximately 80 m with the lower boundary of the inertial sublayer (Wang et al., 2014; Li et al., 2023). Building-resolving LES further shows substantial spatial heterogeneity in mean flow and TKE production across urban roughness-affected heights (Giometto et al., 2016). Wind-tunnel results over realistic morphology distinguish the turbulence scales and momentum-transfer organization of roughness and inertial sublayers (Li et al., 2025). The stronger changes in vertical-velocity variability and mean WS gradient across 47–80 m than across 80–140 m (Section 3.3) place the observed covariance adjustment within an interval of pronounced dynamical variation. The robust signal is therefore not simply a uniform strengthening of turbulence with height: it is a change in how upward and downward motions couple with their temperature anomalies. Such height selectivity is expected in an urban boundary layer where observational levels need not sample dynamically equivalent flow populations.

The distinction between net heat flux and the vertical transport of that flux gives the covariance reorganization its physical significance. In the exact two-branch expansion, the occupancy-weighted within-branch covariances enter the second-order heat flux through their sum. Their imbalance, weighted by the separation of branch-mean vertical velocities, determines the specific covariance

https://doi.org/10.5194/egusphere-2026-6699
Preprint. Discussion started: 13 November 2026
© Author(s) 2026. CC BY 4.0 License.

correction to the branch-based term $k_b F_T$ (Eq. (10b)). Consequently, an increase in the updraft covariance contribution and a decrease in the downdraft contribution can partly compensate in the net heat flux while reinforcing this third-order correction. The opposing 47–80 m covariance contrasts and the concentration of their signed height difference in simultaneous strong motions support this interpretation (Fig. 7). Event composites provide a separate, time-resolved perspective: the vertical-velocity and temperature anomalies have different peak amplitudes and temporal profiles at 47 and 80 m, and these differences are reflected in the event-conditioned third-order transport (Fig. 8). Earlier joint velocity–scalar analyses linked ejection–sweep asymmetry to mixed third-order moments (Ghannam et al., 2017; Li et al., 2018). The present observations add a paired-height perspective by resolving changes in velocity–temperature covariance within rising and sinking motions.

4.2 Implications and limitations

The conditional transport structures identified here provide specific observational constraints for higher-order turbulence representations. Distribution-based and mass-flux approaches describe turbulent transport through different treatments of organized motions and fluctuations within them. Larson and Golaz (2005) derived higher-order moments from assumed joint probability distributions, while Arnold et al. (2026) linked mass-flux contributions to the moments constraining a double-Gaussian distribution. Eddy-diffusivity/mass-flux approaches also distinguish mass-flux transport from turbulence within subdomains (Marcel et al., 2026). These formulations can be evaluated using the observed dependence of conditional temperature anomalies on vertical-motion intensity and buoyancy–shear conditions, together with the height- and site-dependent contributions of within-branch covariance. Examining these properties alongside the total mixed third-order moment would help determine whether models reproduce the underlying conditional transport structure or obtain similar bulk moments through compensating contributions.

The present observations cover quality-controlled unstable conditions, and relaxing the stationarity criterion for M increases the scatter of the bulk relationship (Table S1). Unequal vertical coverage limits direct comparisons of height-dependent transport structures across the three sites. The buoyancy–shear contrasts represent conditional differences, as buoyancy production is calculated using the measured heat flux. Future studies could apply the same conditional diagnostics to independent observations and higher-order closure outputs to evaluate their representation of within-branch transport. Building-resolving large-eddy simulations with controlled variations in surface heating and urban morphology could further clarify the physical processes governing the height-dependent organization of velocity–temperature coupling.

5. Conclusions

Using 10-Hz turbulence observations from the IAP 325 m tower and the Xianghe and Miyun towers, this study examined how rising and sinking motions organize the vertical turbulent transport of heat flux across heights, surface environments and thermomechanical conditions. Bulk moment relationships provided a reference for interpreting this conditional transport.

https://doi.org/10.5194/egusphere-2026-6699
Preprint. Discussion started: 13 November 2026
© Author(s) 2026. CC BY 4.0 License.

The bulk second–third moment relationship remained identifiable across all ten site–height combinations despite contrasting stability responses of the constituent moments. At IAP, R^2 decreased from 0.71 at 47 m to 0.38–0.40 at 140–200 m before recovering to 0.62 at 280 m. Within-branch velocity–temperature covariance made the largest contribution to the residualized thermal pathway at nine combinations. At 280 m, the conditional third-order tail had the larger point estimate, although its ranking relative to covariance was not statistically resolved. The bulk relationship and its internal transport composition thus displayed distinct vertical changes.

At IAP, occupancy-weighted updraft covariance increased from 47 m to 80 m, whereas the downdraft contribution decreased in both years, revealing a reproducible vertical reorganization. Changes in vertical-velocity variability and mean WS gradient were also larger across 47–80 m than across 80–140 m. Simultaneously matched strong vertical motions occupied 13.7% and 13.4% of sampled time but accounted for 76.0% and 66.0%, respectively, of the signed mean height contrast in covariance imbalance. Opposing branch-covariance changes can partly offset in net heat flux while reinforcing the covariance correction to mixed third-order transport. Event composites showed that same-sign vertical motions at 47 and 80 m were accompanied by different temperature anomalies and made unequal contributions to mixed third-order heat transport.

The temperature anomalies carried by vertical motions were not determined by motion intensity alone. At comparable normalized updraft intensities, buoyancy-dominated hours exhibited larger normalized warm anomalies than shear-dominated hours at selected levels in all three environments. During the afternoon, within-updraft thermal coupling weakened at IAP 8–80 m and Miyun, whereas IAP 200–280 m and Xianghe retained comparatively persistent coupling.

Including observed within-branch covariance reduced diagnostic reconstruction RMSE by approximately 50–60% relative to the branch-based reference. Relative to the separately fitted bulk relationship, improvement depended on height, occurring at IAP 8–80 m but not at 200 m. These findings establish that higher-order heat-flux transport has a distinct vertical and conditional organization, reflecting how temperature anomalies are distributed among rising and sinking motions even where a recognizable bulk moment relationship persists.

Data availability

The processed datasets supporting the findings of this study are available from the corresponding author upon reasonable request. Access to the raw high-frequency (10 Hz) sonic anemometer data is subject to approval by the respective data-providing institutions.

Author contributions

LW and YY determined the goal of this study. LW carried it out, performed the data and prepared the paper with contributions from all co-authors. CL, YM, XS and WH contributed to data curation. YY, GZ and WC contributed to the scientific interpretation and manuscript revision. All authors contributed to the improvement of this manuscript and approved the final version of the paper.

Competing interests

https://doi.org/10.5194/egusphere-2026-6699
Preprint. Discussion started: 13 November 2026
© Author(s) 2026. CC BY 4.0 License.

723 The contact author has declared that none of the authors has any competing interests.

724 Acknowledgments

725 We thank all those who contributed to and supported the observations used in this study.

726 Financial support

727 This work has been supported by the National Natural Science Foundation of China (42375076),
728 and the Strategic Priority Research Program of the Chinese Academy of Sciences (Grant No.
729 XDB0760200).

730 References

731 Abdella, K. and McFarlane, N.: A new second-order turbulence closure scheme for the planetary boundary layer, J.
732 Atmos. Sci., 54, 1850–1867, https://doi.org/10.1175/1520-0469(1997)054<1850:ANSOTC>2.0.CO;2, 1997.

733 Abdella, K. and Petersen, A. C.: Third-order moment closure through a mass-flux approach, Bound.-Lay.
734 Meteorol., 95, 303–318, https://doi.org/10.1023/A:1002629010090, 2000.

735 Arnold, N. P., Suselj, K., and Teixeira, J.: A simplified higher order closure + mass flux boundary-layer
736 parameterization in the Goddard Earth Observing System, J. Adv. Model. Earth Sy., 18, e2025MS005701,
737 https://doi.org/10.1029/2025MS005701, 2026.

738 Barlow, J. F.: Progress in observing and modelling the urban boundary layer, Urban Clim., 10, 216–240,
739 https://doi.org/10.1016/j.uclim.2014.03.011, 2014.

740 Barskov, K., Chechin, D., Drozd, I., Artamonov, A., Pashkin, A., Gavrikov, A., Varentsov, M., Stepanenko, V.,
741 and Repina, I.: Relationships between second and third moments in the surface layer under different
742 stratification over grassland and urban landscapes, Bound.-Lay. Meteorol., 187, 311–338,
743 https://doi.org/10.1007/s10546-022-00751-4, 2023.

744 Christen, A., van Gorsel, E., and Vogt, R.: Coherent structures in urban roughness sublayer turbulence, Int. J.
745 Climatol., 27, 1955–1968, https://doi.org/10.1002/joc.1625, 2007.

746 Christen, A., Rotach, M. W., and Vogt, R.: The budget of turbulent kinetic energy in the urban roughness sublayer,
747 Bound.-Lay. Meteorol., 131, 193–222, https://doi.org/10.1007/s10546-009-9359-5, 2009.

748 d'Alençon, L., Hourdin, F., and Rio, C.: Prognostic modeling of total specific humidity variance induced by
749 shallow convective clouds in a GCM, Atmos. Chem. Phys., 26, 7949–7966,
750 https://doi.org/10.5194/acp-26-7949-2026, 2026.

751 De Roo, F. and Mauder, M.: The influence of idealized surface heterogeneity on virtual turbulent flux
752 measurements, Atmos. Chem. Phys., 18, 5059–5074, https://doi.org/10.5194/acp-18-5059-2018, 2018.

753 Dou, J., Grimmond, S., Cheng, Z., Miao, S., Feng, D., and Liao, M.: Summertime surface energy balance fluxes at
754 two Beijing sites, Int. J. Climatol., 39, 2793–2810, https://doi.org/10.1002/joc.5989, 2019.

755 Drozd, I. D., Artamonov, A. Y., Barskov, K. V., Gavrikov, A. V., Pashkin, A. D., Repina, I. A., and Stepanenko,
756 V. M.: Ratio of the second and third turbulent moments in the urban boundary layer of the atmosphere using
757 the example of data from the Moscow State University eddy covariance tower, Izv. Atmos. Ocean. Phys., 59,
758 443–455, https://doi.org/10.1134/S0001433823040151, 2023.

759 Dupont, S. and Patton, E. G.: Momentum and scalar transport within a vegetation canopy following atmospheric
760 stability and seasonal canopy changes: the CHATS experiment, Atmos. Chem. Phys., 12, 5913–5935,
761 https://doi.org/10.5194/acp-12-5913-2012, 2012.

https://doi.org/10.5194/egusphere-2026-6699
Preprint. Discussion started: 13 November 2026
© Author(s) 2026. CC BY 4.0 License.

Efstathiou, G. A., Thuburn, J., and Beare, R. J.: Diagnosing coherent structures in the convective boundary layer by optimizing their vertical turbulent scalar transfer, Bound.-Lay. Meteorol., 174, 119–144, https://doi.org/10.1007/s10546-019-00480-1, 2020.

Finnigan, J.: Turbulence in plant canopies, Annu. Rev. Fluid Mech., 32, 519–571, https://doi.org/10.1146/annurev.fluid.32.1.519, 2000.

Foken, T. and Wichura, B.: Tools for quality assessment of surface-based flux measurements, Agr. Forest Meteorol., 78, 83–105, https://doi.org/10.1016/0168-1923(95)02248-1, 1996.

Ghannam, K., Duman, T., Salesky, S. T., Chamecki, M., and Katul, G. G.: The non-local character of turbulence asymmetry in the convective atmospheric boundary layer, Q. J. Roy. Meteor. Soc., 143, 494–507, https://doi.org/10.1002/qj.2937, 2017.

Giometto, M. G., Christen, A., Meneveau, C., Fang, J., Krafczyk, M., and Parlange, M. B.: Spatial characteristics of roughness sublayer mean flow and turbulence over a realistic urban surface, Bound.-Lay. Meteorol., 160, 425–452, https://doi.org/10.1007/s10546-016-0157-6, 2016.

Golaz, J.-C., Larson, V. E., and Cotton, W. R.: A PDF-based model for boundary layer clouds. Part I: Method and model description, J. Atmos. Sci., 59, 3540–3551, https://doi.org/10.1175/1520-0469(2002)059<3540:APBMFB>2.0.CO;2, 2002.

Gryanik, V. M. and Hartmann, J.: A turbulence closure for the convective boundary layer based on a two-scale mass-flux approach, J. Atmos. Sci., 59, 2729–2744, https://doi.org/10.1175/1520-0469(2002)059<2729:ATCFTC>2.0.CO;2, 2002.

Hersbach, H., Bell, B., Berrisford, P., Hirahara, S., Horányi, A., Muñoz-Sabater, J., Nicolas, J., Peubey, C., Radu, R., Schepers, D., Simmons, A., Soci, C., Abdalla, S., Abellan, X., Balsamo, G., Bechtold, P., Biavati, G., Bidlot, J., Bonavita, M., De Chiara, G., Dahlgren, P., Dee, D., Diamantakis, M., Dragani, R., Flemming, J., Forbes, R., Fuentes, M., Geer, A., Haimberger, L., Healy, S., Hogan, R. J., Hólm, E., Janisková, M., Keeley, S., Laloyaux, P., Lopez, P., Lupu, C., Radnoti, G., de Rosnay, P., Rozum, I., Vamborg, F., Villaume, S., and Thépaut, J.-N.: The ERA5 global reanalysis, Q. J. Roy. Meteor. Soc., 146, 1999–2049, https://doi.org/10.1002/qj.3803, 2020.

Kaimal, J. C., Wyngaard, J. C., Haugen, D. A., Coté, O. R., Izumi, Y., Caughey, S. J., and Readings, C. J.: Turbulence structure in the convective boundary layer, J. Atmos. Sci., 33, 2152–2169, https://doi.org/10.1175/1520-0469(1976)033<2152:TSITCB>2.0.CO;2, 1976.

Katul, G. G., Hsieh, C.-I., Kuhn, G., Ellsworth, D., and Nie, D.: Turbulent eddy motion at the forest–atmosphere interface, J. Geophys. Res.-Atmos., 102, 13409–13421, https://doi.org/10.1029/97JD00777, 1997.

Kljun, N., Calanca, P., Rotach, M. W., and Schmid, H. P.: A simple two-dimensional parameterisation for Flux Footprint Prediction (FFP), Geosci. Model Dev., 8, 3695–3713, https://doi.org/10.5194/gmd-8-3695-2015, 2015.

Lappen, C.-L. and Randall, D. A.: Toward a unified parameterization of the boundary layer and moist convection. Part II: Lateral mass exchanges and subplume-scale fluxes, J. Atmos. Sci., 58, 2037–2051, https://doi.org/10.1175/1520-0469(2001)058<2037:TAUPOT>2.0.CO;2, 2001.

Larson, V. E. and Golaz, J.-C.: Using probability density functions to derive consistent closure relationships among higher-order moments, Mon. Weather Rev., 133, 1023–1042, https://doi.org/10.1175/MWR2902.1, 2005.

Li, B., Han, Z., Zhang, X., Yang, Q., Li, C., and Sun, L.: Investigation of the vertically-layered structure and surface roughness parameters of the urban boundary layer, Struct. Des. Tall Spec. Build., 32, e2056, https://doi.org/10.1002/tal.2056, 2023.

Li, D. and Bou-Zeid, E.: Coherent structures and the dissimilarity of turbulent transport of momentum and scalars in the unstable atmospheric surface layer, Bound.-Lay. Meteorol., 140, 243–262, https://doi.org/10.1007/s10546-011-9613-5, 2011.

https://doi.org/10.5194/egusphere-2026-6699
Preprint. Discussion started: 13 November 2026
© Author(s) 2026. CC BY 4.0 License.

Li, D., Katul, G. G., and Liu, H.: Intrinsic constraints on asymmetric turbulent transport of scalars within the constant flux layer of the lower atmosphere, Geophys. Res. Lett., 45, 2022–2030, https://doi.org/10.1002/2018GL077021, 2018.

Li, F., Wang, R., Chen, G., Mo, Z., Ikegaya, N., and Liu, C.-H.: Turbulence scale and strength analysis in the roughness and inertial sublayers over urban areas: A wind tunnel study, Build. Environ., 267, 112193, https://doi.org/10.1016/j.buildenv.2024.112193, 2025.

Liu, H., Gao, Z., and Katul, G. G.: Non-closure of surface energy balance linked to asymmetric turbulent transport of scalars by large eddies, J. Geophys. Res.-Atmos., 126, e2020JD034474, https://doi.org/10.1029/2020JD034474, 2021.

Marcel, A., Riette, S., Ricard, D., and Lac, C.: An update of shallow cloud parameterization in the AROME NWP model, Atmos. Chem. Phys., 26, 3901–3932, https://doi.org/10.5194/acp-26-3901-2026, 2026.

Miao, S., Dou, J., Chen, F., Li, J., and Li, A.: Analysis of observations on the urban surface energy balance in Beijing, Sci. China Earth Sci., 55, 1881–1890, https://doi.org/10.1007/s11430-012-4411-6, 2012.

Park, S.-B. and Baik, J.-J.: A large-eddy simulation study of thermal effects on turbulence coherent structures in and above a building array, J. Appl. Meteorol. Clim., 52, 1348–1365, https://doi.org/10.1175/JAMC-D-12-0162.1, 2013.

Petersen, A. C., Beets, C., van Dop, H., Duynkerke, P. G., and Siebesma, A. P.: Mass-flux characteristics of reactive scalars in the convective boundary layer, J. Atmos. Sci., 56, 37–56, https://doi.org/10.1175/1520-0469(1999)056<0037:MFCORS>2.0.CO;2, 1999.

Raupach, M. R., Finnigan, J. J., and Brunet, Y.: Coherent eddies and turbulence in vegetation canopies: The mixing-layer analogy, Bound.-Lay. Meteorol., 78, 351–382, https://doi.org/10.1007/BF00120941, 1996.

Rotach, M. W.: On the influence of the urban roughness sublayer on turbulence and dispersion, Atmos. Environ., 33, 4001–4008, https://doi.org/10.1016/S1352-2310(99)00141-7, 1999.

Rotach, M. W., Vogt, R., Bernhofer, C., Batchvarova, E., Christen, A., Clappier, A., Feddersen, B., Gryning, S.-E., Martucci, G., Mayer, H., Mitev, V., Oke, T. R., Parlow, E., Richner, H., Roth, M., Roulet, Y.-A., Ruffieux, D., Salmond, J. A., Schatzmann, M., and Voogt, J. A.: BUBBLE—an urban boundary layer meteorology project, Theor. Appl. Climatol., 81, 231–261, https://doi.org/10.1007/s00704-004-0117-9, 2005.

Roth, M.: Turbulent transfer relationships over an urban surface. II: Integral statistics, Q. J. Roy. Meteor. Soc., 119, 1105–1120, https://doi.org/10.1002/qj.49711951312, 1993.

Roth, M.: Review of atmospheric turbulence over cities, Q. J. Roy. Meteor. Soc., 126, 941–990, https://doi.org/10.1002/qj.49712656409, 2000.

Siebesma, A. P., Soares, P. M. M., and Teixeira, J.: A combined eddy-diffusivity mass-flux approach for the convective boundary layer, J. Atmos. Sci., 64, 1230–1248, https://doi.org/10.1175/JAS3888.1, 2007.

Sun, Q., Zhang, L., Xue, J., Wang, L., Li, Y., and Yang, Y.: Comparison of turbulent transport dissimilarity and the role of coherent structures in the unstable surface layer between urban and rural areas, Bound.-Lay. Meteorol., 192, 34, https://doi.org/10.1007/s10546-026-00978-5, 2026.

Theeuwes, N. E., Ronda, R. J., Harman, I. N., Christen, A., and Grimmond, C. S. B.: Parametrizing horizontally-averaged wind and temperature profiles in the urban roughness sublayer, Bound.-Lay. Meteorol., 173, 321–348, https://doi.org/10.1007/s10546-019-00472-1, 2019.

Wang, L., Li, D., Gao, Z., Sun, T., Guo, X., and Bou-Zeid, E. R.: Turbulent transport of momentum and scalars above an urban canopy, Bound.-Lay. Meteorol., 150, 485–511, https://doi.org/10.1007/s10546-013-9877-z, 2014.

Wang, L., Gao, Z., Miao, S., Guo, X., Sun, T., Liu, M., and Li, D.: Contrasting characteristics of the surface energy balance between the urban and rural areas of Beijing, Adv. Atmos. Sci., 32, 505–514, https://doi.org/10.1007/s00376-014-3222-4, 2015.

https://doi.org/10.5194/egusphere-2026-6699
Preprint. Discussion started: 13 November 2026
© Author(s) 2026. CC BY 4.0 License.



Wang, S. and Stevens, B.: Top-hat representation of turbulence statistics in cloud-topped boundary layers: A large eddy simulation study, J. Atmos. Sci., 57, 423–441, https://doi.org/10.1175/1520-0469(2000)057<0423:THROTS>2.0.CO;2, 2000.

Yang, J. and Huang, X.: 30 m annual land cover and its dynamics in China from 1990 to 2019 (Version 1.0.0), Zenodo [dataset], https://doi.org/10.5281/zenodo.4417810, 2021a.

Yang, J. and Huang, X.: The 30 m annual land cover dataset and its dynamics in China from 1990 to 2019, Earth Syst. Sci. Data, 13, 3907–3925, https://doi.org/10.5194/essd-13-3907-2021, 2021b.

Zhou, K., Liu, C.-H., and Wan, M.: Large-scale coherent structure and canopy-level turbulence in the convective boundary layer over urban areas, Build. Environ., 244, 110733, https://doi.org/10.1016/j.buildenv.2023.110733, 2023.

Zilitinkevich, S., Gryanik, V. M., Lykossov, V. N., and Mironov, D. V.: Third-order transport and nonlocal turbulence closures for convective boundary layers, J. Atmos. Sci., 56, 3463–3477, https://doi.org/10.1175/1520-0469(1999)056<3463:TOTANT>2.0.CO;2, 1999.